Experimental evidence of the wind-induced bias of precipitation gauges using Particle Image Velocimetry and particle tracking in the wind tunnel

Article *in* Journal of Hydrology · July 2021

DOI: 10.1016/j.jhydrol.2021.126690

5 authors, including:

Arianna Cauteruccio
University of Genova
14 PUBLICATIONS **49** CITATIONS

Elia Brambilla
Politecnico di Milano
14 PUBLICATIONS **22** CITATIONS

Mattia Stagnaro
Università degli Studi di Genova
24 PUBLICATIONS **188** CITATIONS

Luca G Lanza
Università degli Studi di Genova
143 PUBLICATIONS **2,680** CITATIONS

Journal of Hydrology 600 (2021) 126690

Contents lists available at ScienceDirect

Journal of Hydrology

journal homepage: www.elsevier.com/locate/jhydrol

Research papers

Experimental evidence of the wind-induced bias of precipitation gauges using particle image velocimetry and particle tracking in the wind tunnel

Arianna Cauteruccio[a], Elia Brambilla[b], Mattia Stagnaro[a], Luca G. Lanza[a,c,*], Daniele Rocchi[b]

[a] Department of Civil, Chemical and Environmental Engineering, University of Genova, Genoa, Italy
[b] Department of Mechanical Engineering, Politecnico di Milano, Milan, Italy
[c] WMO/CIMO Lead Centre "B. Castelli" on Precipitation Intensity, Italy

ARTICLE INFO

This manuscript was handled by Marco Borga, Editor-in-Chief, with the assistance of Francesco Marra, Associate Editor

Keywords:
Rainfall
Rain gauges
Wind
Measurement bias
Wind tunnel
PIV
Wind-induced bias

ABSTRACT

Wind tunnel (WT) experiments were conducted to reproduce the wind-induced deviation of rain drop trajectories when approaching the collector of catching-type gauges. Three typical outer shapes of the instrument body (cylindrical, inverted-conical and "chimney" shapes) were tested using full-scale models. The airflow pattern upstream of and above the collector was measured with a Particle Image Velocimetry technique, after injecting a passive tracer in the flow. Tests were performed by releasing water drops in the WT flow to mimic the raindrops fall. The drop trajectories near the gauge collector were tracked and quantitatively measured using a high-speed camera. The deviation of the trajectories, induced by the bluff-body aerodynamics of the gauge, is interpreted here by comparing the measured airflow pattern around the three instruments to highlight the effect of their different outer shapes. The "chimney" shape, that is typical of some weighing type gauges, demonstrated lower performance with respect to the cylindrical and inverted-conical shape, showing the most relevant effect in deviating the trajectories of the approaching drops when immersed in a wind field.

1. Introduction

Aiming at the measurement of essential environmental variables, atmospheric precipitation is one of the most challenging and accurate measurements are not easily obtained (see Cauteruccio et al., 2021a for a review of in-situ precipitation measurement issues). Both instrumental and environmental sources of bias and uncertainty are inherent of the precipitation measurement process. When precipitation occurs in windy conditions, a systematic bias in measurements – often termed the "wind-induced undercatch" – is to be expected for all catching-type instruments.

Jevons (1861) was among the first to identify the so called "exposure problem", which produces underestimation of precipitation measurements due to the vertical velocity component and acceleration that arise in front of and above the gauge collector when the gauge is exposed to the wind.

Since then, the problem of the wind induced bias on precipitation measurements was addressed in the literature following different approaches: field tests (see e.g. Pollock et al., 2018; Wolff et al., 2015), numerical simulations using Computational Fluid Dynamics (CFD) (see e.g. Nešpor and Sevruk, 1999; Colli et al., 2015; Colli et al., 2018) and wind tunnel (WT) experiments (see e.g. Green and Helliwell, 1972; Robinson and Rodda, 1969).

Among the influencing factors – including e.g., the particle size distribution, precipitation intensity, the shape, density and fall velocity of hydrometeors, etc. – the outer shape of the gauge was shown to have a prevailing role by acting as a bluff-body obstacle to the incoming wind.

For this reason, wind tunnel testing of the aerodynamics of precipitation gauges has been a suitable investigation tool in precipitation measurement studies.

Since the early work of Bastamoff and Witkiewitch (1926), most studies mainly concentrated on identifying design solutions, such as rain gauges shape optimization (Strangeways, 2004) or windshields (Alter, 1937), to minimize the airflow acceleration and updraft and therefore the impact of the gauge body on the surrounding wind field.

For example, Sanuki et al. (1952) tested two types of windshields for rain gauges (conical and hollow ring-shaped designs) both in a water tank and in the WT. The test was conducted at free-stream velocity ranging from 1.5 to 20 m/s and the flow patterns were photographed after spreading aluminum powder over the water surface of the tank and using wool strings tied to the model in the WT. Air speed measurements in the WT were taken above the funnel mouth at a height equal to 0.5

---

[*] Corresponding author at: Department of Civil, Chemical and Environmental Engineering, University of Genova, Genoa, Italy.
E-mail address: luca.lanza@unige.it (L.G. Lanza).

https://doi.org/10.1016/j.jhydrol.2021.126690

times the diameter of the gauge orifice. In these experiments the minimum generation of eddies in all parts of the flow field was sought for the assessment of the windshield design.

Robinson and Rodda (1969) examined the airflow pattern around four types of rain gauges in a series of WT experiments using tuft indicators, smoke trajectories and hot-wire anemometer measurements for quantitative assessment of the wind velocity over the gauges. Two cylindrical gauges, one gauge characterized by a bluff shape and one with champagne glass shape were studied. All gauges exhibited similar aerodynamic behavior, characterized by a separation zone starting from the leading edge and curving over the collector. The wind speed reaches a maximum above the separation zone, while below it the flow velocity drops, and a turbulent zone develops. Observations identified the wind speed at which a clear lift of the smoke at the top of the gauges is evident. The height of the lift of the smoke trajectory above the gauge appeared to increase with increasing diameter of the gauge and with increasing sharpness of the leading edge of the collector for equal wind speed. The authors concluded that the two cylindrical gauges appeared to produce the least satisfactory airflow patterns. The more complex bluff shape and the champagne glass shape caused less distortion of the wind field.

In the most recent works of Cauteruccio et al. (2020, 2021b) and Nešpor and Sevruk (1999), WT measurements of the flow velocity were obtained by employing multi-hole pressure probes located in selected positions above the investigated gauge geometries, at different wind speeds, with the objective to validate numerical CFD simulations.

The wind-induced undercatch derives from the impact of the airflow deformation on the trajectories of water drops when approaching the collector. Once the microphysical characteristics of precipitation, particle size distribution, precipitation intensity, and the deviation of each hydrometeor trajectory from the undisturbed one, are known, suitable models can be used to derive adjustment curves for operational use (see e.g., Cauteruccio and Lanza, 2020). To provide evidence of this phenomenon, more complex WT tests that combines wind speed and the presence of hydrometeors were carried out in the past.

Warnik (1953) injected real (dry and low-density) and sawdust snow into the WT to visualize the airflow pattern and to study the quantitative catch of the model gauges. Wind speed from 5 to 10 m/s were tested. For the first time the trajectories of precipitating solid particles under windy conditions and their deviations when approaching the gauge were visualized, although not precisely measured. Just the overall undercatch was quantitatively obtained with the main objective to justify the inconsistencies observed in records of snow catch in the field. Results were also used to design the geometry of two windshields.

Green and Helliwell (1972), measured both airflow velocity profiles and water drop trajectories above a cylindrical rain gauge. The flow field was measured using hotwire anemometers positioned on a grid, while the trajectories of injected drops were tracked using photographs from a still reflex camera. Trajectories of water drops, with diameters of 1.2, 2.2 and 3.5 mm, were recorded with low details. An apparent catchment area, defined by the positions reached by two deflected drop trajectories which, in undisturbed conditions, would aim to the upwind and downwind edges of the collector, was used to calculate the gauge catch. This assumption implies that the most deflected trajectory aims, in undisturbed conditions, to the leeward edge of the collector, which is neither known a priori nor necessarily true.

Besides the observed wind-induced bias of catching-type precipitation gauges in the field, and the available technical solutions used to limit its impact on the measurement accuracy, there is a need for quantitative experimental evidence, obtained in fully controlled conditions (laboratory or WT tests), of the physical processes acting behind the exposure problem and their respective role.

This work presents, for the first time to the authors knowledge, two joint quantitative pieces of evidence of the wind-induced bias of catching-type gauges in controlled WT conditions. The first is a detailed assessment of the airflow configuration upstream of and above the gauge collector and the second is the resulting deviation of drop trajectories when approaching the gauge, both obtained by video tracking techniques. Interpretation of the drop behavior was therefore possible based on the measured airflow pattern, and the impact of different outer shapes of commercially available precipitation gauges on the catch efficiency is compared in the following.

2. Methodology

Experiments were carried out in the large-scale WT facility available at the Politecnico di Milano (hereafter GVPM) within the activities of the Italian national project PRIN 20154WX5NA “Reconciling precipitation with runoff: the role of understated measurement biases in the modelling of hydrological processes”. Three typical outer shapes of commercial rain gauges were investigated to assess their aerodynamic characteristic and the resulting effect on the trajectories of the approaching hydrometeors, namely the cylindrical, the “chimney” and the inverted-conical shapes. Most tipping-bucket rain gauges available on the market have indeed a cylindrical geometry, the most common weighing gauges have a typical chimney shape (due to the large amount of rainwater stored to avoid the need of frequently emptying the gauge), while the so-called “aerodynamic” gauges have an innovative inverted-conical shape (although they too are based on the tipping-bucket mechanism). The commercial models adopted in this research were therefore the *Lambrecht Rain[e]H3©* (although this instrument is actually a hybrid tipping-bucket and weighing gauge), the *Geonor T200B©* and the *EML SBS500©*, assumed as representative specimens for the cylindrical, chimney and inverted-conical shape, respectively.

The experiments consisted of two steps: first a Particle Image Velocimetry (PIV) technique was used to measure the airflow pattern upstream of and above the gauge collector, then drops were released in the WT to mimic raindrops falling in a windy environment. The drop trajectories near the gauge collector were tracked and quantitatively measured using a high-speed camera.

The PIV technique provided the flow velocity pattern on a 2-D (x, z) section of the flow field (where x is the stream-wise direction and z the vertical coordinate) centered on the longitudinal symmetry axis of the collector. A castor oil smoke was injected in the WT and used as a passive tracer, while the measurement section was illuminated with a light sheet produced by a pulsed laser emitter (output energy 200 mJ) using a cylindrical optics with an aperture of 50°. The upper part of the gauges was painted in black to avoid the reflection of light and suitable masking of the captured images was adopted to post process the PIV acquisitions. Pictures were taken using a double-shutter camera with a 50 mm optics, equipped with a 2 MPx (1953 × 1112 px) CCd sensor, positioned at about 2 m from the measurement section. The latter had dimensions 435 × 250 mm with a magnification factor of 4.34 px/mm.

The frame rate of the acquisition was 100 microseconds, and two hundred pairs of images were captured to guarantee sufficient statistical significance of the post process analysis. Images were processed with the Pivview 2C© software, produced by PIVTEC GmbH in collaboration with the German Aerospace Center (DLR). The processing algorithm was set to single correlation analysis on partially (50%) overlapping windows of 64 × 64 pixels, therefore obtaining a resolution of about 7 mm per each measurement position. The accuracy can be evaluated based on a positioning uncertainty of 0.1 pixels corresponding, under the conditions of this test, to an uncertainty on the velocity equal to 0.2 m/s. The outputs of the single acquisitions were averaged over the total number of images to obtain an average flow field under steady flow conditions. For each precipitation gauge, tests were conducted at wind speeds equal to 5 and 10 m s^{-1} and the flow velocity fields were discretized into a regular grid with cell size of 7.5 × 7.5 mm.

A dedicated experimental setup was designed and realized in the GVPM to measure the deviation of drop trajectories when they are approaching and travelling above the gauge collector. Water drops were released in the WT flow upstream the gauge and their trajectories were captured with a high-speed camera in the vertical 2-D plane centered on the longitudinal symmetry axis of the gauge collector. The experimental setup is described in detail in Cauteruccio (2020) and Cauteruccio et al. (2021b).

The recording speed was set to 1000 fps, with an image resolution of 1600 × 900 pixels. The captured footages were about 40 × 20 cm wide, with a pixel size between 0.19 and 0.24 mm, depending on the single test. The videos recorded by the camera were analyzed in the MATLAB® environment, where the path of each drop was identified. To improve the visibility of the drops, each image was converted to greyscale and Gaussian and Laplacian filters were applied. The image was binarized so as to report the background with zeroes and the position of the drop with ones. Finally, a moving window was used over the image to identify and record the center of the drop. From the time interval between two subsequent images and the dimension of each pixels, the drop speed was calculated.

3. Results and discussion

Results about the airflow velocity fields are shown in the form of color-coded maps of the normalized vertical velocity component and plots of the normalized positions of the maximum velocity values obtained from the PIV. The maps confirm previous literature works (Colli et al., 2016; Colli et al., 2018) about the scalability (low Reynolds dependency) of the airflow fields, except for the chimney-shaped gauge for undisturbed wind velocity, U_{ref}, between 5 and 10 m s^{-1}, as detailed below. In addition, local velocity flow measurements previously obtained at the University of Genova, and used to validate CFD airflow simulation results (Cauteruccio et al., 2021b), show that the normalized velocity components are fairly scalable, especially in the range between 10 and 20 m s^{-1}. An example of the low Reynolds dependency of the profiles of the normalized vertical flow velocity, U_z/U_{ref}, along the central stream-wise symmetry plane above the gauge collector is reported in Fig. 1, for the three outer geometries investigated in this work.

The scalability of the flow field allows us to apply the PIV results to a wider range of wind velocities, both lower and higher than the experimental range. Drop trajectories observed at wind speed from 9 to 13 m s^{-1}, are shown and commented according to the PIV velocity fields measured at 10 m s^{-1}, together with the derived slope curves. In the graphs below, the drop trajectories are depicted in the dimensionless plane x/D and z/D, where D is the gauge collector diameter (equal to 0.16 m for the *Lambrecht Rain[e]H3©* and the *GeonorT200B©* gauges, and equal to 0.25 m for the *EML-SBS500©* gauge) and the gauge collector is centered in (0, 0). For each gauge, the longitudinal coordinate (x/D) of the drop releasing position was fixed while the elevation (z/D) was set according to the wind speed.

3.1. Airflow velocity fields

The color-coded maps of the normalized vertical velocity component (U_z/U_{ref}) presented in Fig. 2 show that, for the chimney-shaped and the cylindrical gauges, upward velocity components are present along the entire collector while, for the inverted-conical gauge, downward velocity components prevail in the region above the second half-part of the collector. It is evident from the graphs that the maximum updraft (a bit larger than 0.7) is associated with the *Geonor-T200B©* gauge, due to the chimney shape of the gauge body, while the cylindrical gauge, the *Lambrecht Rain[e]H3©*, has the least pronounced updraft value. The *EML-SBS500©* gauge exhibits the maximum downdraft.

Anticipating the influence that these vertical components would have on the trajectories of approaching hydrometeors, it must be considered that the balance between the updraft and downdraft above the gauge collector is the relevant takeover information, useful to compare different gauge shapes. Indeed, the hydrometeor trajectories will be deflected upward – depending on their shape and vertical velocity – when the vertical velocity is positive (updraft), while they will tend to recover their original undisturbed trajectory when the vertical velocity is negative (downdraft). From the airflow velocity maps it can be noted that the chimney-shaped gauge is the one producing the most unbalanced vertical forces, with a predominant upward component and a low downward component while, consistently with the work of Cauteruccio et al. (2020), for the inverted-conical gauge in uniform free-stream conditions, the updraft in the upwind part of the collector and the downdraft in the downwind part are comparable in magnitude. The behavior of the cylindrical gauge is intermediate.

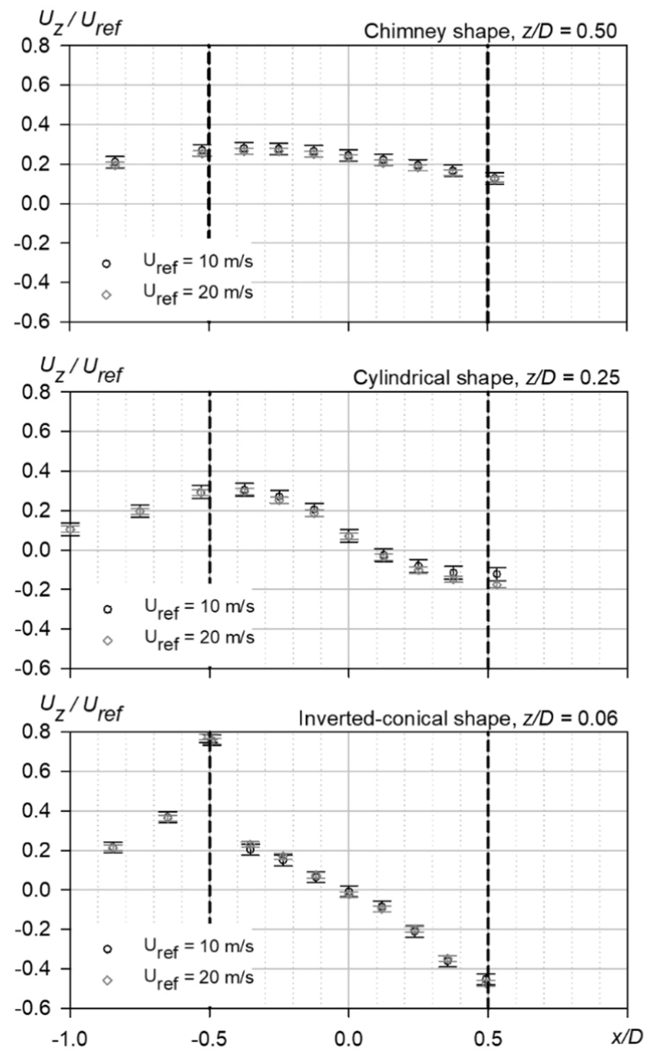

Fig. 1. Normalized vertical velocity profiles, U_z/U_{ref}, measured by velocity probes along the central stream-wise symmetry plane above the collector of precipitation gauges having the three investigated outer geometries. Measurements are taken at U_{ref} = 10 and 20 m s^{-1} and at various normalized elevation (z/D, with D the collector diameter) to show the low Reynolds dependency of the flow field induced by the presence of the gauge.

Fig. 3 reports the normalized positions of the maximum velocity values obtained from PIV measurements at U_{ref} = 5 m s^{-1} for the three geometries investigated. This result reveals that these positions are higher and more dispersed for the chimney-shaped *Geonor-T200B©* gauge, while they are lower and more bounded for the inverted-conical shape. The behavior of the cylindrical gauge is intermediate.

In Fig. 4 a-c the normalized positions of the maximum velocity values for each gauge geometry at U_{ref} = 5 (triangles) and 10 (circles) m s^{-1} are compared, and color coded based on the normalized magnitude of the airflow velocity (U_{mag}/U_{ref}). The magnitude of flow velocity is larger for the gauge with inverted-conical shape and lower for the other two

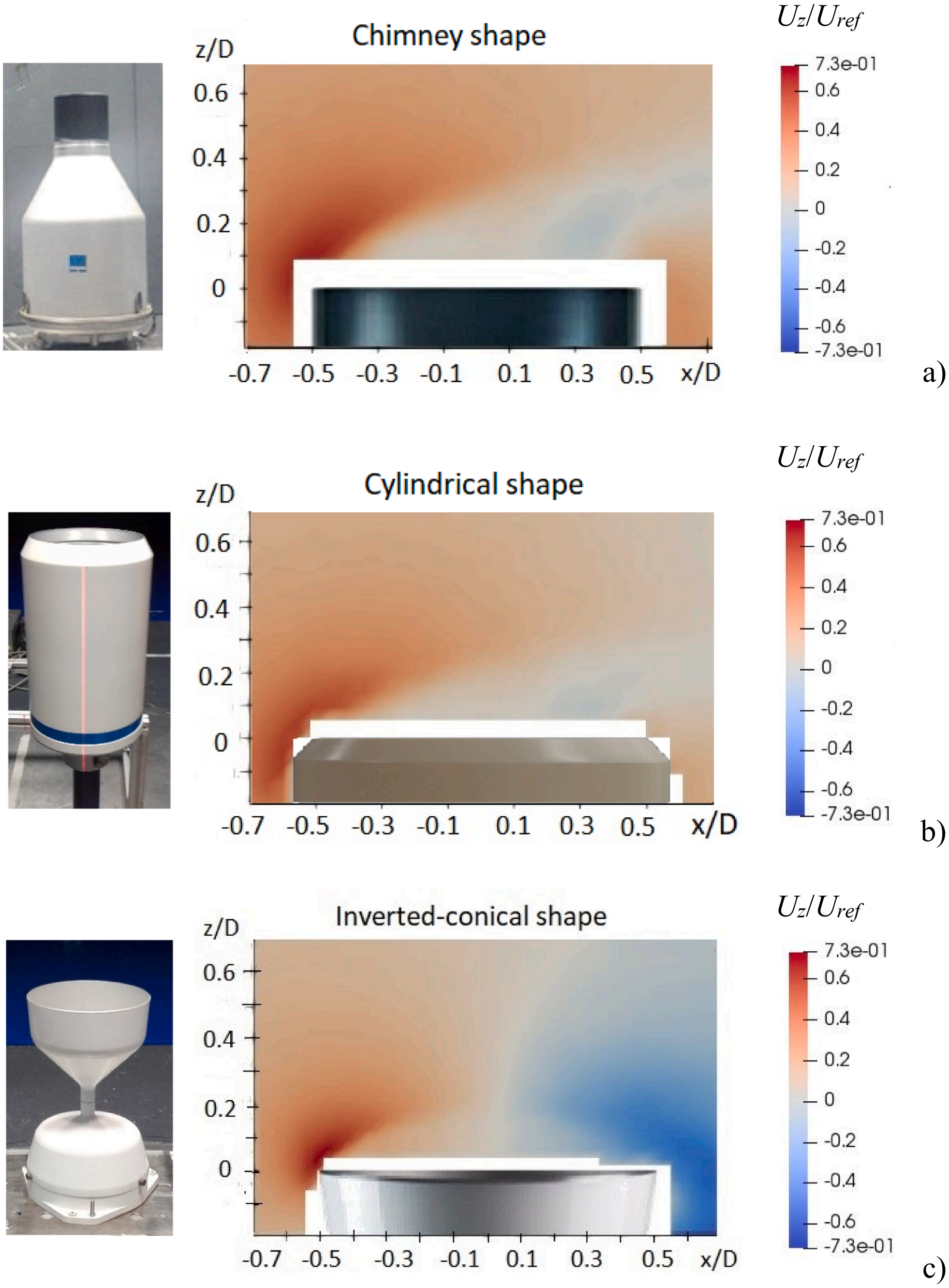

Fig. 2. Photographs of the three investigated gauges installed in the WT and PIV fields of the normalized vertical velocity component (U_z/U_{ref}) in the central ($y/D = 0$) stream-wise section at $U_{ref} = 10$ m s^{-1}, for chimney-shaped (a), cylindrical (b) and inverted-conical (c) gauges.

geometries. Moreover, for the chimney-shaped gauge the non-dimensional maximum velocity patterns show a Reynolds number dependency (their normalized positions do not overlap upon varying the flow velocity) both in terms of normalized velocity magnitude and positions.

3.2. Observed drop trajectories

The WT experimental campaign resulted in capturing 106 trajectories of drops released between $|z/D| = 0.18$ and $|z/D| = 0.70$ above the *Lambrecht Rain[e]H3©* (at $U_{ref} = 8.9$ to 13.1 m s^{-1}), 82 trajectories of drops released between $|z/D| = 0.05$ and $|z/D| = 0.70$ above the *GeonorT200B©* (at $U_{ref} = 8.86$ to 13.6 m s^{-1}), and 50 trajectories of drops released between $|z/D| = 0.15$ and $|z/D| = 0.60$ above the *EML-SBS500©* gauge (at $U_{ref} = 9.35$ to 12.6 m s^{-1}). For each gauge geometry and wind speed, drops of different size were generated and the obtained drop diameter ranges between 0.9 and 1.2 mm. These values were derived from images captured by the video camera during dedicated tests conducted in still air.

In this section, sample observed drop trajectories are selected and illustrated to discuss their relevant features, together with the associated slope curves. In the following, the prefix CH identifies the *GeonorT200B©* chimney-shaped gauge, while CY and IC indicate the cylindrical and inverted-conical shape of the *Lambrecht Rain[e]H3©* and *EML-SBS500©* gauges, respectively.

Repeatability was checked for trajectories (and their deviation) having the closest initial positions and for all gauges. In Fig. 5, the Root-Mean-Square Deviation (RMSD) of pairs of trajectories is reported as a

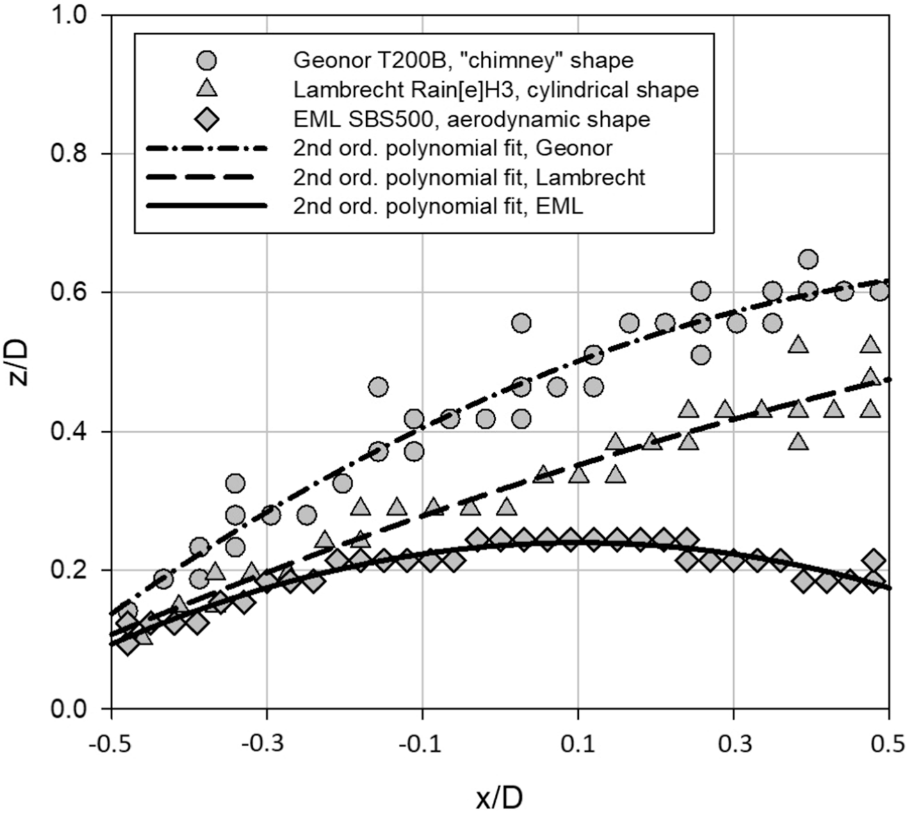

Fig. 3. Normalized positions of the maximum velocity values obtained from PIV measurements at $U_{ref} = 5$ m s^{-1}, for the chimney (circles), cylindrical (triangles) and inverted-conical (diamonds) shapes, in the central ($y/D = 0$) stream-wise section. The upwind edge of the collector is in (-0.5,0).

function of the vertical distance between their initial positions (only those with very close initial positions are shown). Trajectories observed for all three gauges are included and differentiated using different markers. It is shown that the RMSD is always lower, with very few exceptions, than the maximum estimated size of the drop in the observed trajectories (1.2 mm), highlighted by the dashed horizontal line. The markers also show a clear trend towards smaller RMSD while decreasing the distance of the initial position of each pair of trajectories, which strongly confirms their repeatability. This is an important feature of our experiment since not only it implies that the experimental setup was correctly implemented, but also confirms that the deviation induced by wind on the drop trajectory is systematic, beside some measurement uncertainties due to the inherent limitations of the video tracking system.

An example of one observed drop trajectory, above the collector of the chimney-shaped gauge at $U_{ref} = 12.8$ m s^{-1}, is indicated with markers in the top panel of Fig. 6. The first part of the observed trajectory, depicted with triangles, is not affected by the aerodynamic response of the gauge and can be linearly extrapolated (solid line in the graph) to obtain the undisturbed trajectory (dashed line in the graph extended to the maximum longitudinal coordinate of the observed trajectory wherever $z/D > 0$). The disturbed part of the trajectory, depicted with circles, was fitted with a third-order polynomial (dotted line in the graph). The slope curve (dz/dx, see the solid line in the bottom panel of Fig. 6) was obtained as the first derivative of the fitted trajectory and compared in the same plot with the slope curve of the undisturbed trajectory (horizontal dashed line). When the drop approaches the collector of the gauge it enters the region of the flow field with significant vertical velocity components and its trajectory deviates from the undisturbed one. Moreover, from the comparison between observed and undisturbed trajectories it is evident that the undisturbed trajectory would enter the collector while the observed one overtakes the collector and travels beyond the gauge, therefore highlighting the phenomenon of the wind-induced undercatch.

In the following figures, some further examples of observed drop trajectories are reported and organized in pairs for each investigated gauge. In order to interrelate the drop position with the airflow deformation induced by the gauge body, the normalized positions of the maximum velocity values measured by the PIV technique are depicted with light blue lines.

Fig. 7 reports a pair of observed trajectories for two drops (named CH3 and CH6) having the same size – as demonstrated by the undisturbed slope – and released approximatively at the same initial position above the *Geonor T200B©* gauge at $U_{ref} = 10.2$ m s^{-1}. Similar trajectories and the associated slope curves are reported in Fig. 8 for two drops (CY97 and CY98) having approximatively the same size and travelling above the collector of the gauge with cylindrical shape, at $U_{ref} = 13.1$ m s^{-1}. In both figures, the drops released at a higher elevation start later to deviate from the undisturbed trajectory and are less sensitive to the recirculating zone in the second half part of the collector.

Drops of different size (therefore with different undisturbed slope) were also observed at the same wind velocity, and their trajectories are shown, for instance, in Fig. 9 for the inverted-conical gauge at $U_{ref} = 11.6$ m s^{-1}. As demonstrated by the slope curves (continuous lines) the drop depicted in red (IC84) is larger than the green one (IC81). Note that, for all gauges, the deviation of the actual trajectories from the undisturbed ones becomes visually evident when they cross the pattern of the maximum velocity values (light blue line).

3.3. Comparison between PIV and observed drop trajectories

Wind-induced deviations of the trajectories vary with the shape of the gauge and are consistent with the analysis of the velocity field of the recirculation zone in the various cases.

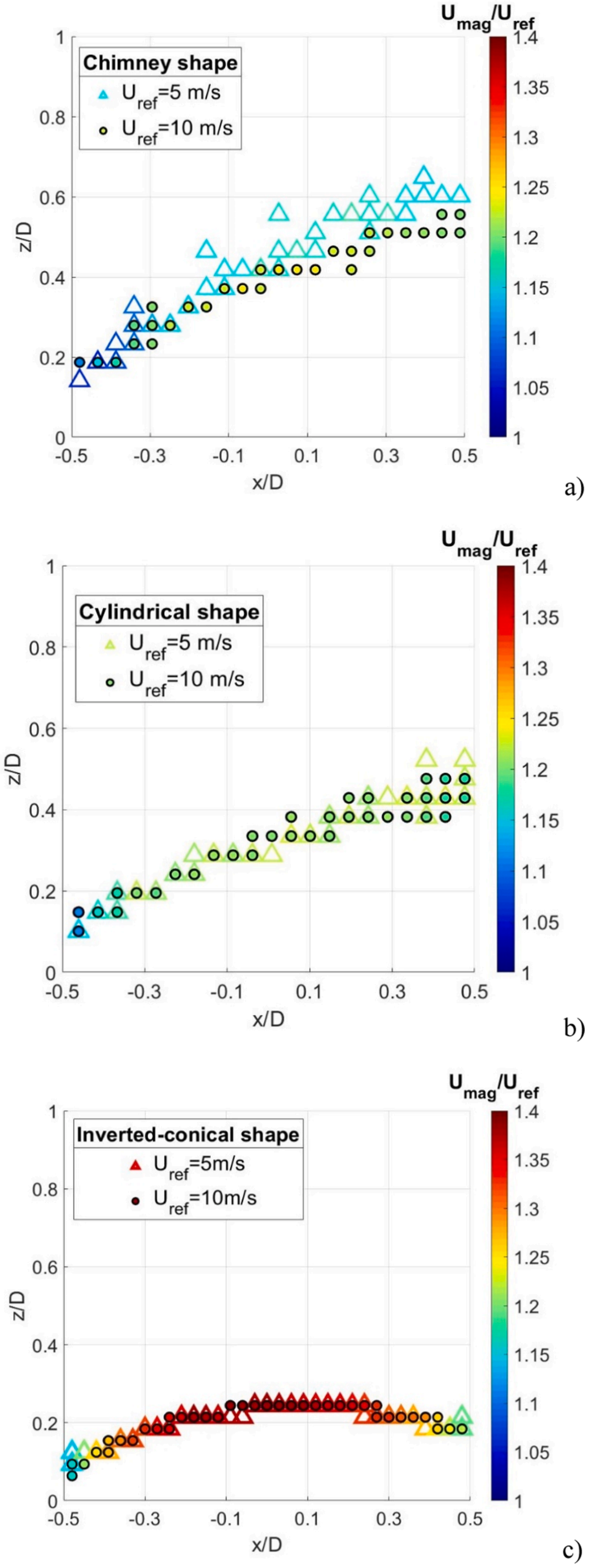

Fig. 4. Dimensionless positions (x/D, z/D) of the maximum flow velocity magnitude (U_{mag}/U_{ref}) obtained from the PIV in the central ($y/D = 0$) streamwise section, for the chimney-shaped (a), cylindrical (b) and inverted-conical (c) gauges at $U_{ref} = 5$ (triangles) and 10 (circles) m s^{-1}. The upwind edge of the collector is in (−0.5,0).

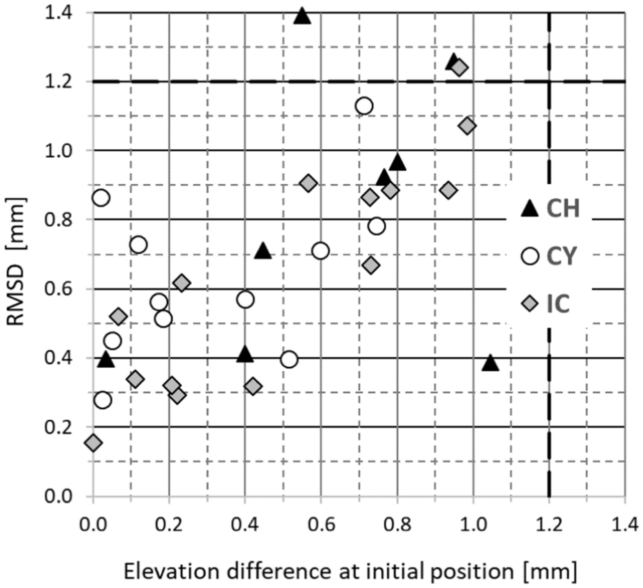

Fig. 5. Repeatability of the observed deviations expressed in terms of the RMSD of pairs of trajectories having the closest elevation difference at their initial position. Dashed lines indicate the maximum estimated size of the drops released during the experiment.

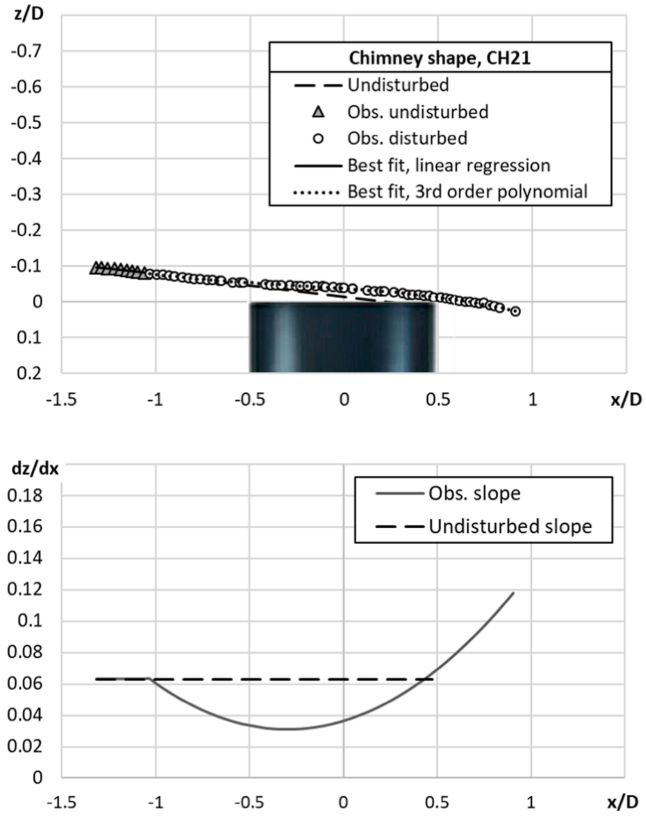

Fig. 6. Observed (markers) and undisturbed (dashed line) drop trajectory above the collector of the chimney-shaped gauge (top panel) at $U_{ref} = 12.8$ m s^{-1}, and the associated slope curves for both trajectories (bottom panel).

In this section, we show and compare three drops (named CH11, CY31 and IC83), which in undisturbed conditions should hit the downwind part of the gauge collector but are deviated by the aerodynamic interference of the gauge. Their disturbed trajectories are commented in relation with the measured PIV velocity field. The

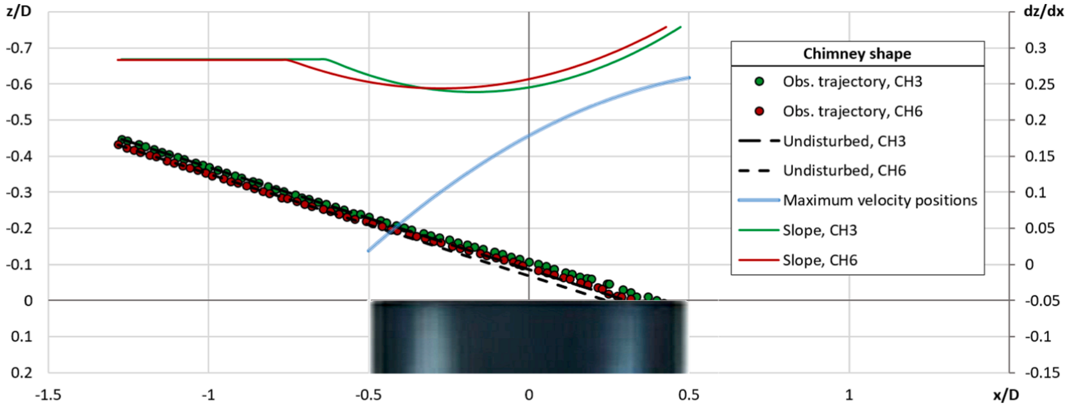

Fig. 7. Pair of drops having approximately the same size (circles) and associated slope curves (continuous lines) travelling above the collector of the chimney-shaped gauge at $U_{ref} = 10.2$ m s^{-1}.

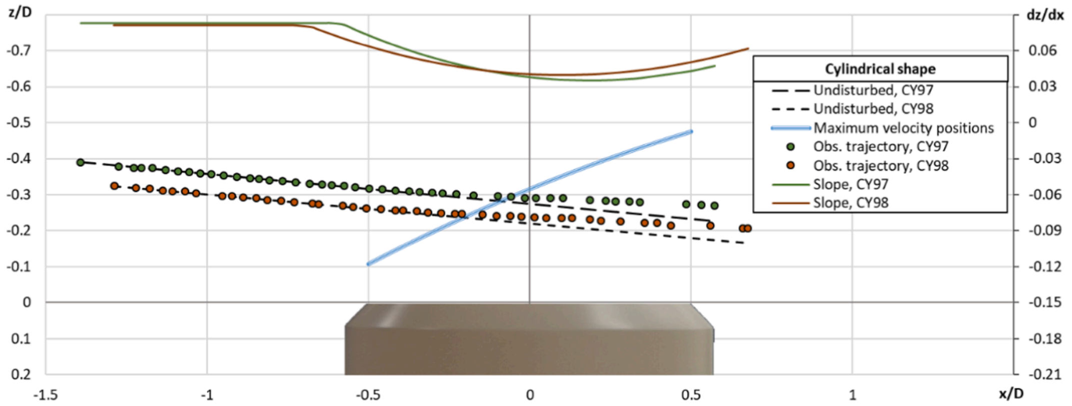

Fig. 8. Pair of drops having approximately the same size (circles) and associated slope curves (continuous lines) travelling above the collector of the cylindrical gauge at $U_{ref} = 13.1$ m s^{-1}.

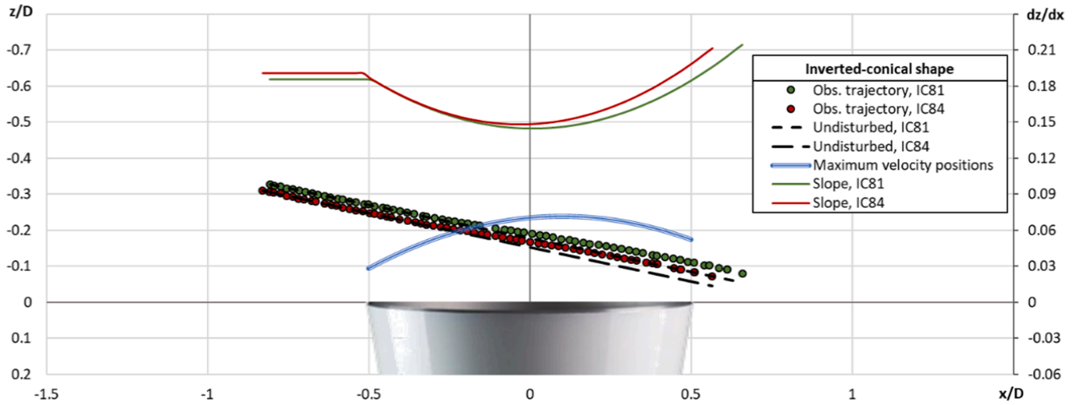

Fig. 9. Pair of drops (circles) and associated slope curves (continuous lines) travelling above the collector of the inverted-conical gauge at $U_{ref} = 11.6$ m s^{-1}.

Table 1
Wind speed and starting position for the three analyzed drop trajectories and the associated gauge geometry.

Gauge shape	Diameter *D* [m]	ID	U_{ref} [m s^{-1}]	Initial position	
				x/D	*z/D*
Chimney	0.160	CH11	11.40	−1.31926	−0.29778
Cylindrical	0.160	CY31	12.10	−1.38060	−0.26418
Inverted-conical	0.252	IC83	11.16	−0.79748	−0.27044

Table 2
Parameters of the linear regression (m and q) for the undisturbed trajectories and of the third order polynomial for the disturbed ones (a, b, c and d), with the associated correlation factor.

ID	m	q	R^2	a	b	c	d	R^2
CH11	0.1733	−0.0681	0.9985	0.0263	0.0138	0.1301	−0.0995	0.9998
CY31	0.1411	−0.0711	0.997	0.0293	0.0223	0.1133	−0.0921	0.9981
IC83	0.1991	−0.111	0.9965	0.0504	0.0100	0.1495	−0.1329	0.9999

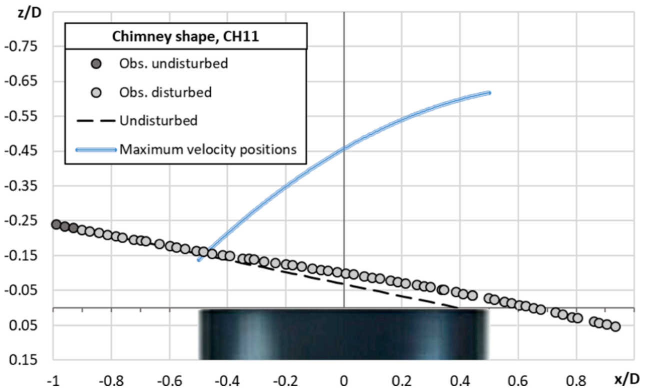

Fig. 10. Observed drop trajectory named CH11 (circles) and the undisturbed one (dashed line) above the collector of the gauge with chimney shape at $U_{ref} = 11.4$ m s^{-1}.

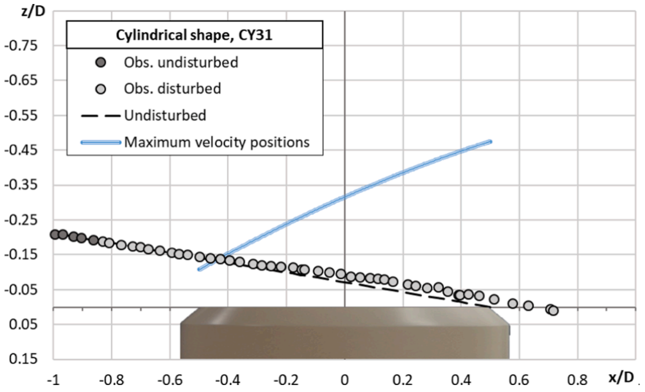

Fig. 11. Observed drop trajectory named CY31 (circles) and the undisturbed one (dashed line) above the collector of the gauge with cylindrical shape at $U_{ref} = 12.1$ m s^{-1}.

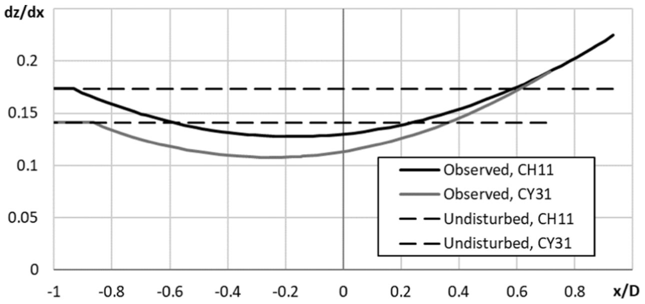

Fig. 12. Comparison between the slope curves for two drops travelling above the gauges with cylindrical (at $U_{ref} = 12.1$ m s^{-1}) and chimney (at $U_{ref} = 11.4$ m s^{-1}) shape (having the same size of the collector), for the observed (solid line) and undisturbed (dashed line) trajectories.

compared drop trajectories were chosen by minimizing the relative difference between the respective starting positions (z/D) at the same free-stream airflow velocity (U_{ref}). These data are listed in Table 1. The parameters of the best-fit curves describing the trajectories of the drops, and the associated correlation factors (R^2) are listed in Table 2.

Figs. 10 and 11 report the observed drop trajectories CH11 and CY31, which travel above the collector of the chimney-shaped and cylindrical gauges, respectively. In Fig. 12 their slopes are compared with the undisturbed ones. In both cases, when the drop trajectories approach the gauge collector (at x/D = -0.5) they visually deviate from the undisturbed trajectory and their slope decreases. Moreover, the two drops fall outside instead of inside of the collector, therefore highlighting the very nature of the wind-induced undercatch affecting precipitation measurements.

The collectors of the chimney-shaped and cylindrical gauges have the same size, while the collector of the inverted-conical gauge is larger. Therefore, the features of trajectories CH11 and CY31 are better comparable. The injection system was maintained at a fixed distance from the center of the gauge collector, therefore drops were released closer to the gauge with inverted-conical shape than for the other two gauges.

In Fig. 13 a sample drop trajectory travelling above the inverted-conical gauge is depicted together with the associated slope curve. The effect of the comparability between the airflow updraft and downdraft for this geometry, as discussed above, can be observed here by noting that the deviation of the drop trajectory is almost totally bounded within the region delimited by the projection of the collector edges (x/D = ± 0.5, Fig. 13 bottom panel).

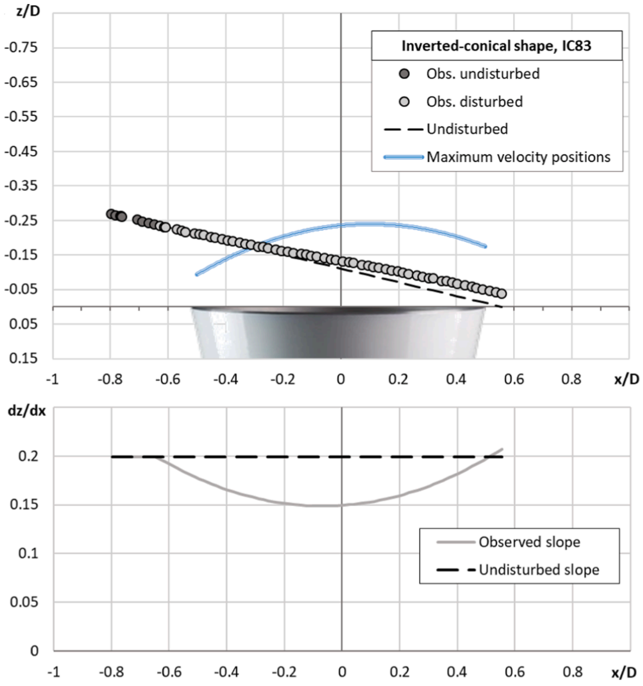

Fig. 13. Observed drop trajectory named IC83 (circles) and the undisturbed one (dashed line) above the collector of the inverted-conical gauge (top panel) at $U_{ref} = 11.16$ m s^{-1}, and the associated slope curves for both trajectories (bottom panel).

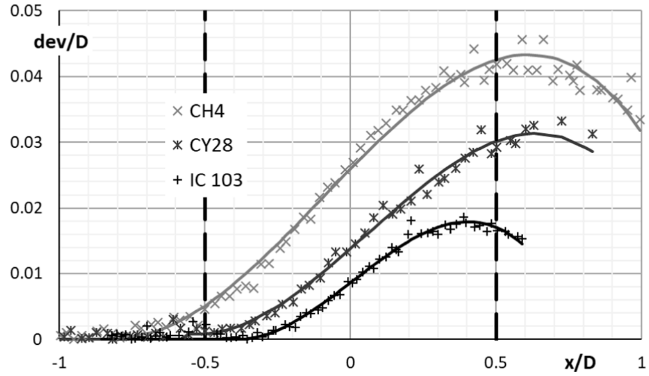

Fig. 14. Observed normalized deviations from the undisturbed trajectory of drops released with similar size and position above the collector of the three types of gauge shape investigated. Deviations indicated with markers are calculated from the measured drop positions, while solid lines are calculated from the interpolated polynomial trajectories. Vertical dashed lines indicate the position of the edges of the collector.

Consistently with the PIV velocity field, the slope of the trajectory in the downwind part of the collector increases faster for the cylindrical gauge than for the chimney-shaped gauge (see Fig. 12). Moreover, the wind speed for the trajectory that travels above the collector of the chimney-shaped gauge ($U_{ref} = 11.4$ m s^{-1}) is lower than for the trajectory captured above the cylindrical gauge ($U_{ref} = 12.1$ m s^{-1}) and the undisturbed slopes suggest that the size of the drop observed above the chimney-shaped gauge is larger than the one that travels above the cylindrical gauge. These results suggest that the aerodynamic behaviour of the chimney-shaped gauge could be the most negatively impactful on the collection performance of the gauge (yielding a larger undercatch).

The normalized deviation, *dev/D,* of each observed drop trajectory from the undisturbed one is quantitatively measured by calculating the distance from the geometrical position of the drop at each time step to the straight line representing the undisturbed trajectory (extrapolated from the initial observed positions of the drop). This yields a curve as a function of the longitudinal coordinate, departing from zero when the drop starts deviating from the undisturbed trajectory (due to the airflow updraft and acceleration) and reaching a maximum distance beyond which the drop starts approaching again the original path, since the slope of its trajectory increases (due to the airflow downdraft and deceleration).

Due to the experimental variability of the obtained drop size and releasing position, few trajectories can be found that allow consistent comparison of the three outer shapes investigated in this work, i.e., drops that, with the same size and at the same wind speed, are released precisely in the same normalized position relative to the upwind edge of the gauge collector.

One example is provided in Fig. 14, where the comparison of similar drop trajectories for the three outer shapes investigated is shown in terms of their deviations, *dev/D*. Markers indicate deviations calculated from the measured drop positions, while solid lines are calculated from the interpolated polynomial trajectories. The graph shows that the deviations are significantly different in the three cases, with the chimney-shaped gauge having the most relevant deviation throughout the whole trajectory, the cylindrical gauge being intermediate, and the inverted-conical gauge having the least deviated pattern. As reported in Table 3, the normalised deviations at the downwind edge of the collector ($x/D = 0.5$) also follow the same order, and the longitudinal coordinate at which the drop starts deviating from the undisturbed trajectory increases when moving from the CH to the CY and IC gauge shapes, according to the more extended influence of the gauge aerodynamic behaviour.

This is fully consistent with the previous observations and the airflow velocity patterns revealed by the PIV and confirms that the chimney-shaped gauge has the worst performance when compared with the cylindrical and inverted-conical shapes.

4. Conclusions

The obtained quantitative experimental evidence of the deviation of drop trajectories when approaching the collector of catching-type gauges in controlled WT conditions provides insights into the physical processes acting behind the exposure problem and their respective role in affecting the trajectories of hydrometeors having various size and fall velocity. This will support the development of both correction algorithms for the wind-induced bias of precipitation measurements and optimal gauge/windshield geometries for operational use.

Using video tracking techniques, contemporary quantitative evidence of the wind-induced bias of catching-type gauges was indeed provided in this work, by means of a detailed assessment of both the airflow pattern upstream and above of the gauge collector and the resulting deviation of the injected drop trajectories when approaching the gauge. Interpretation of the drop behavior was therefore possible based on the measured airflow pattern, and the impact of different outer shapes of commercially available precipitation gauges on the catch efficiency was compared.

The data collected are also a reliable data set for validation of numerical CFD models of the flow field and the particle trajectories (Cauteruccio et al., 2021b), allowing a theoretically based derivation of correction curves and the analysis of the most influencing factors and controlling variables. This was hardly possible hitherto based on the experimental evidence obtained from field test sites alone, where the many external factors contemporarily acting on the gauge catch usually mask the underlying physical process with a high level of noise. To reduce the spreading of experimental data around the expected theoretical behavior, better identification of the controlling variables is needed, and their effect individually quantified, which is only possible in fully controlled experiments.

Using the obtained dataset (here provided as supplementary material) as a benchmark to validate numerical models is also an added value of the present work. Indeed, the availability of a large size WT facility with a water drop releasing device and a particle tracking system is not usual but it represents an interesting special research infrastructure specifically developed in the framework of the Italian national project PRIN 20154WX5NA. The present research is part of a wider activity aiming at quantifying the undercatch effect induced by the wind on gauges and to define their collection efficiency. The proposed methodology consists in using the experimental WT results to set-up and

Table 3
Characteristics of the trajectories of drops with similar size and releasing position depicted in Fig. 14, and quantitative parameters of their deviation for the three outer shapes investigated.

ID	U_{ref} [m s^{-1}]	*dz/dx* undisturbed	*x/D* detachment	*dev/D* at $x/D = 0.5$	*dev* [mm]
CH4	10.20	0.265	−0,740	0.043	6.8
CY28	10.60	0.241	−0.556	0.030	4.8
IC103	9.85	0.292	−0.338	0.017	4.3

validate numerical CFD simulations under laboratory controlled conditions, while investigating more realistic environmental conditions through CFD simulations in order to consider the characteristics of rainfall (drop size distribution, shape, etc.) and wind in the atmospheric boundary layer (velocity, turbulence intensity, length scale, etc.). The proposed experimental/numerical methodology would be useful for the instrument design and calibration, allowing for a gauge shape optimization or the adoption of mitigation solution by looking not only at the aerodynamic performance but also at the measuring performance.

The tests performed in controlled WT experiments allowed to compare instruments with three different outer shapes of the gauge body, under the same wind forcing and drop releasing conditions. Representative specimens for the cylindrical, chimney and inverted-conical shape were tested, confirming the good performance of the "aerodynamic" solution. The chimney shape, that is typical of some weighing type gauges, demonstrated lower performance with respect to the cylindrical and inverted-conical shape, showing the most relevant effect in deviating the trajectories of the approaching water drops when immersed in a wind field.

Further developments of this work could be focused on examining additional aerodynamic features of the gauge body, such as the sharpness of the collector's rim and the relative dimensions of the various parts of the outer geometry of the gauge. Also, the experimental setup could be improved by developing an injection system able to release drops with an initial velocity component close to their terminal velocity. However, we believe that numerical simulation, properly calibrated using the observations presented in this work, would be the most promising approach to address such and similar issues.

CRediT authorship contribution statement

Arianna Cauteruccio: Conceptualization, Methodology, Software, Validation, Investigation, Writing - original draft, Writing - review & editing. **Elia Brambilla:** Methodology, Software, Investigation, Writing - review & editing. **Mattia Stagnaro:** Conceptualization, Methodology, Investigation, Writing - review & editing. **Luca G. Lanza:** Conceptualization, Methodology, Investigation, Writing - review & editing, Supervision, Project administration. **Daniele Rocchi:** Conceptualization, Methodology, Investigation, Writing - review & editing, Supervision.

Declaration of Competing Interest

The authors declare that they have no known competing financial interests or personal relationships that could have appeared to influence the work reported in this paper.

Acknowledgements

This work was developed in the framework of the Italian national project PRIN20154WX5NA "Reconciling precipitation with runoff: the role of understated measurement biases in the modelling of hydrological processes", and as partial fulfilment of the PhD thesis of the first author.

Appendix A. Supplementary data

Supplementary data to this article can be found online at https://doi.org/10.1016/j.jhydrol.2021.126690 and also at http://www.precipitation-biases.it/Drop-Trajectories-JHydrol2021.php.

References

Alter, J.C., 1937. Shielded storage precipitation gages. Mon. Wea. Rev. 65 (7), 262–265. https://doi.org/10.1175/1520-0493(1937)65<262:SSPG>2.0.CO;2.

Bastamoff, S.L., Witkiewitch, W.J., 1926. Les spectres aerodynamiques des pluviometres. Bull. Geophysique de L'Institut des Recherches Geophyssiqes 10.

Cauteruccio, A., 2020. The role of turbulence in particle-fluid interaction as induced by the outer geometry of catching-type precipitation gauges. PhD Thesis. University of Genova, Italy. https://doi.org/10.15167/cauteruccio-arianna_phd2020-04-06 (Accessed 16 July 2021).

Cauteruccio, A., Brambilla, E., Stagnaro, M., Lanza, L.G., Rocchi, D., 2021b. Wind tunnel validation of a particle tracking model to evaluate the wind-induced bias of precipitation measurements. Water Resour. Res. 57 (7). https://doi.org/10.1029/2020WR028766. e2020WR028766.

Cauteruccio, A., Colli, M., Freda, A., Stagnaro, M., Lanza, L.G., 2020. The role of free-stream turbulence in attenuating the wind updraft above the collector of precipitation gauges. J. Atmos. Oceanic Technol. 37 (1), 103–113. https://doi.org/10.1175/JTECH-D-19-0089.1.

Cauteruccio, A., Colli, M., Stagnaro, M., Lanza, L.G., Vuerich, E., 2021a. In situ precipitation measurements. In: Foken, T. (Ed.), Handbook of Atmospheric Measurements. Springer Nature, Switzerland, pp. 259–400. https://doi.org/10.1007/978-3-030-51171-4_12.

Cauteruccio, A., Lanza, L.G., 2020. Parameterization of the collection efficiency of a cylindrical catching-type rain gauge based on rainfall intensity. Water 12 (12), 3431. https://doi.org/10.3390/w12123431.

Colli, M., Lanza, L.G., Rasmussen, R., Thériault, J.M., Baker, B.C., Kochendorfer, J., 2015. An improved trajectory model to evaluate the collection performance of snow gauges. J. Appl. Meteor. Climatol. 54 (8), 1826–1836. https://doi.org/10.1175/JAMC-D-15-0035.1.

Colli, M., Lanza, L.G., Rasmussen, R., Thèriault, J.M., 2016. The collection efficiency of shielded and unshielded precipitation gauges. Part I: CFD airflow modelling. J. of Hydrometeorol. 17 (1), 231–243. https://doi.org/10.1175/JHM-D-15-0010.1.

Colli, M., Pollock, M., Stagnaro, M., Lanza, L.G., Dutton, M., O'Connell, E., 2018. A Computational Fluid-Dynamics assessment of the improved performance of aerodynamic raingauges. Water Resour. Res. 54 (2), 779–796. https://doi.org/10.1002/2017WR020549.

Green, M.J., Helliwell, P.R., 1972. The effect of wind on the rainfall catch. Distribution of precipitation in mountainous areas. *World Meteorological Organization,* Rep. 326, Vol. 2, 27–46.

Jevons, W.S., 1861. On the deficiency of rain in an elevated rain-gauge, as caused by wind. The London, Edinburgh, and Dublin Philosophical Magazine and Journal of Science 22 (149), 421–433. https://doi.org/10.1080/14786446108643180.

Nešpor, V., Sevruk, B., 1999. Estimation of wind-induced error of rainfall gauge measurements using a numerical simulation. J. Atmos. Ocean. Technol. 16 (4), 450–464. https://doi.org/10.1175/1520-0426(1999)016,0450:EOWIEO.2.0.CO;2.

Pollock, M.D., O'Donnell, G., Quinn, P., Dutton, M., Black, A., Wilkinson, M.E., Colli, M., Stagnaro, M., Lanza, L.G., Lewis, E., Kilsby, C.G., O'Connell, P.E., 2018. Quantifying and mitigating wind-induced undercatch in rainfall measurements. Water Resour. Res. 54 (6), 3863–3875. https://doi.org/10.1029/2017WR022421.

Robinson, A.C., Rodda, J.C., 1969. Rain wind and aerodynamic characteristics of rain-gauges. Meteorol. Mag. 98, 113–120.

Sanuki, M., Tsuda, N., Kimura, S., 1952. Water tank and wind tunnel tests on rain gauge wind shield. *Pap. Met. Geophys.*, Tokyo 3 (1), 54–63.

Strangeways, I., 2004. Improving precipitation measurement. Int. J. Climatol. 24 (11), 1443–1460. https://doi.org/10.1002/joc.1075.

Warnik, C.C., 1953. Experiments with windshields for precipitation gages. Transactions of the American Geophysical Union 34 (3), 379–388. https://doi.org/10.1029/TR034i003p00379.

Wolff, M.A., Isaksen, K., Petersen-Øverleir, A., Ødemark, K., Reitan, T., Brækkan, R., 2015. Derivation of a new continuous adjustment function for correcting wind-induced loss of solid precipitation: results of a Norwegian field study. Hydrol. Earth Syst. Sci. 19 (2), 951–967. https://doi.org/10.5194/hess-19-951-2015.